

# Optical-domain spectral super-resolution enabled by a quantum memory

Mateusz Mazelanik,<sup>1,2</sup> Adam Leszczyński,<sup>1,2</sup> and Michał Parniak<sup>1,3,\*</sup>

<sup>1</sup>*Centre for Quantum Optical Technologies, Centre of New Technologies,  
University of Warsaw, Banacha 2c, 02-097 Warsaw, Poland*

<sup>2</sup>*Faculty of Physics, University of Warsaw, Pasteura 5, 02-093 Warsaw, Poland*

<sup>3</sup>*Niels Bohr Institute, University of Copenhagen, Blegdamsvej 17, 2100 Copenhagen, Denmark*

Existing super-resolution methods of optical imaging hold a solid place as an application in multiple sciences, but many new developments allow beating of diffraction limit in better and more subtle ways. An avenue was opened by suggesting to fully exploit information already present in the field by performing quantum-inspired tailored measurements. Here we exploit the full *spectral* information of the optical field in order to beat the Rayleigh limit in spectroscopy. We employ optical quantum memory with spin-wave storage and an embedded processing capability to implement a time-inversion interferometer for input light, projecting the optical field in the symmetric–anti-symmetric mode basis. Our tailored measurement achieves a resolution of 15 kHz and requires 20.1 times less photons than a corresponding Rayleigh-limited conventional method. We demonstrate the advantage of our technique over both conventional spectroscopy and heterodyne measurements, showing potential for application in distinguishing ultra-narrowband emitters, optical communication channels, or signals transduced from lower-frequency domains.

Optical spectroscopy is an indispensable tool in the studies of matter and light, covering chemistry [1, 2], astronomy [3], biology and medicine [4], metrology, and more. Yet, the resolution of all state-of-the-art methods, such as grating-based [5, 6] and Fourier spectrometers [7–9], is subject to the Rayleigh limit. Methods of beating this limit are widely known in the context of imaging and include modifying, or exploiting very specific properties of the source or illumination [10–13], which is often infeasible. Furthermore, even though the Rayleigh limit has been originally formulated in the context of a spectroscopy [14], super-resolution methods of spectroscopy are scarce and limited to laser spectroscopy [15]. The task and challenges of fluorescence spectroscopy are starkly different: a typical emitter provides only a small photon number per single spectro-spatial mode, which is a strong incentive to seek quantum-enhanced protocols.

In imaging, the modern understanding of the Rayleigh limit is formulated as a vanishing information about separation of two sources for small separations, termed the “Rayleigh curse”. *Tsang et al.* [16] have noticed that the quantum Cramér-Rao bound (Q-CRB), which identifies maximum information available in the optical field, is not saturated by traditional methods. This work inspired new methods that allow reaching the quantum limit [17–23], most recently also in the time domain [24, 25]. The idea to apply an analogous protocol for spectroscopy faces challenges, especially if operation with narrowband optical signal is desired. Yet, the inspiration can be drawn from another domain: in the nuclear-magnetic resonance (NMR) spectroscopy a quantum memory can lead to increased resolution when sensing with color centers in diamond [26–28]. A general framework for those experiments has been formulated by *Gefen et al.* [29] who identified specific

quantum measurements that facilitate super-resolution. A resulting idea is therefore to use a quantum memory to achieve spectral super-resolution in the optical domain.

Here we bring the quantum-inspired super-resolution methods to the spectral domain and demonstrate a device that can resolve frequency differences of two emitters with precision below the Rayleigh limit. Our method utilizes a Gradient Echo Memory (GEM) with built-in time-frequency processing capabilities which we program to realize a pulse-division time-axis-inversion (PuDTAI) interferometer. Our protocol operates in the ultra-narrowband domain, achieving a resolution of 15 kHz with simultaneous super-resolution enhancement factor of  $s = 20.05$  which means that 20.05 times less photons are needed to achieve the same resolution as direct spectroscopy with the same aperture.

Our work not only establishes a new super-resolution spectroscopy method, but also provides an exceptionally good spectral resolution in absolute terms. Fundamentally, this super-resolving method exploits the spectral information already present in light, not requiring specific properties of source or illumination. Such performance is enabled by the long coherence time of the spin-wave quantum memory which serves to extract the quantum information from the optical field in an optimal way.

The conjunction of the operation in the optical domain and the kHz-level resolution has promising application in the schemes that combine microwave or radio-frequency and optical domains [30]. Our method of spectroscopy can provide an optimal detection scheme for light that is transduced from the RF or microwave domain, without the sensitivity loss due to shot noise, which is inherently present in the traditional heterodyne optical receivers.

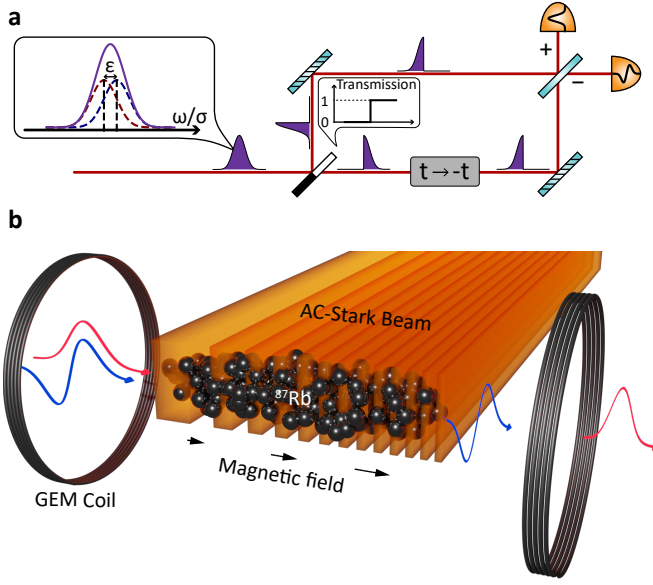


**FIG. 1. Protocol idea and experimental setup.** **a** The task is to measure a separation between two spectral lines. Separation is smaller than the linewidths, which are determined by the properties of the source itself or by the aperture of the spectroscopic measurement device. The signal pulse is sent to the pulse-division time-axis-inversion (PuDTAI) interferometer to separate its symmetric and anti-symmetric parts. First, a time-dependent-transmission mirror splits the pulse in half between the two interferometer arms. One of the arms includes a time inversion device that mirrors the first half of the pulse. Finally, the two components are combined on a beamsplitter, and the resulting symmetric (+) and antisymmetric (-) projections are detected. **b** Experimental realization with a cold-atoms ensemble. The Gradient Echo Memory (GEM) device with symmetrically-chirped (Control detuning) control field maps the signal pulse onto atomic ground-state coherence of  $^{87}\text{Rb}$  atoms and simultaneously implements the time-dependent-transmission mirror and time-inversion transformation. AC-Stark phase modulation with chirped square wave gratings (AC-S Gratings) is used to implement the beamsplitter operation and sequentially read-out the resulting interferometer ports. The full sequence is shown in Extended Data Figure 5.

### Protocol

Let us first set the stage of the problem before introducing the protocol itself. Two mutually incoherent sources with equal brightness emit photons with the same spectral envelope  $\tilde{\psi}(\omega)$  that is assumed to be known, and is the Fourier transform of the time-domain envelope  $\psi(t)$ . Such scenario is relevant both for the cases of fluorescence (with photon pulses being determined by spontaneous emission, assuming fast excitation and no inhomogeneous broadening) and scattering (such as Raman scattering, where we may need to consider relative phases of ground-state coherences). It is also an optical analogue of the radio-frequency-domain physics

present in spectrum analyzers and nano-NMR [29].

A more conventional, but equally relevant scenario is when the linewidths of two sources are very narrow, and the resolution is limited by an aperture, which sets the transfer function  $\tilde{\psi}(\omega)$ . In our case, this would be a Gaussian aperture controlled by how the quantum memory device stores light. In particular, the shape of the control field pulse would set the stored pulse shape  $\psi(t)$ .

The two sources in question have slightly different central frequencies  $\omega_- = \omega_0 - \delta\omega/2$  and  $\omega_+ = \omega_0 + \delta\omega/2$ , where the frequency separation  $\delta\omega = \sigma\varepsilon$  is smaller than the width  $\sigma$  of the spectral envelope  $\tilde{\psi}(\omega)$  that for the normalized separation parameter  $\varepsilon$  translates to  $\varepsilon \ll 1$ . The spectroscopist's task is to estimate the separation  $\varepsilon$  with maximum efficacy - to obtain maximum information about the separation per collected photon.

The idea for achieving sub-Rayleigh performance in our spectrometer via the PuDTAI protocol relies on engineering a measurement that can split the signal pulse into symmetric and anti-symmetric combinations with respect to the mean time or frequency. The protocol that realizes this projective measurement is inspired by a technique known from conventional (real space) super-resolved imaging called SLIVER (superlocalization via image-inversion interferometry) [21, 22, 31–33], where an image is inverted in one arm of a Mach-Zehnder interferometer. In our protocol, schematically depicted in Fig. 1a we divide the signal in half, rather than splitting the signal to prepare two identical copies. This method while being slightly different from SLIVER, achieves the same sensitivity to source separation and inherently, as an additional feature, allows use with  $N$ -photon states [34].

To experimentally implement the PuDTAI interferometer that is schematically depicted in 2a we employ spectro-temporal manipulations in an atomic Gradient Echo Memory [35–37]. The experimental setup is depicted in Fig. 1b. A strong control field  $\mathcal{C}$  maps the signal pulses with slowly varying amplitude  $\mathcal{A}(t)$  onto atomic coherence  $\varrho_{hg}(z)$ . The coherence is then phase-modulated using spatially-varying light shifts, and finally is converted back to light. The crucial feature of the GEM protocol is the spectro-spatial mapping that links spectral components of the signal pulse with the amplitude of the atomic coherence along the ensemble  $\tilde{\mathcal{A}}(\omega) \leftrightarrow \varrho_{hg}(z)$ . At the same time, in time domain, the pulse shape is transferred to wavevector-space components of the coherence  $\mathcal{A}(t) \leftrightarrow \tilde{\rho}_{hg}(k_z)$ . The most convenient way to understand evolution of the atomic coherence at each step of the protocol is to investigate a phase-space quasi-probability given by the Wigner function

$$\mathcal{W}(z, k_z) = \frac{1}{\sqrt{2\pi}} \int \varrho_{hg}(z + \xi/2) \varrho_{hg}^*(z - \xi/2) \exp(-ik_z \xi) d\xi \quad (1)$$

which becomes inherently linked to a chronocyclic Wigner function [38] describing the signal pulse.

Two complementary transformations are applied sequentially to implement the protocol: a temporal and spectral phase modulation. The temporal modulation is realized during the mapping procedure by modulating the two-photon detuning  $\delta$ . Explicitly, a modulation  $\delta \rightarrow \delta(t)$  virtually applies a temporal phase profile  $\mathcal{A}(t) \rightarrow \mathcal{A}(t) \exp(i \int \delta(t) dt)$  onto the signal pulse. At the same time, distinct spectral components of the pulse are mapped onto different positions in the atomic medium  $\tilde{\mathcal{A}}(\omega) \rightarrow \varrho_{hg}(z)$ , when the time shape is transferred to wavevector space  $\mathcal{A}(t) \rightarrow \tilde{\rho}_{hg}(k_z)$ . Thus, temporal phase modulations are linked to  $z$ -direction reshaping of the quasiprobability  $\mathcal{W}(z, k_z) \xrightarrow{\delta(t)} \mathcal{W}(z', k_z)$ .

The spectro-spatial mapping enables implementation of spectral phase operations by phase-modulating the coherence in real-space coordinates  $\varrho_{hg}(z) \rightarrow \varrho(z) \exp(i\chi(z))$ . For this, we use Spatial Spin-wave Modulation (SSM) [39–41], that allows imprinting arbitrary phase profiles onto the coherence. These are linked to  $k_z$ -direction reshaping of the Wigner function  $\mathcal{W}(z, k_z) \xrightarrow{\chi(z)} \mathcal{W}(z, k'_z)$ .

Within this framework, we are able to realize both the time-dependent-transmission mirror that divides the pulse and performs a time-inversion as well as beamsplitter that combines the two components and performs the final projection. The step-by-step evolution of the quasiprobability  $\mathcal{W}(z, k_z)$  in our protocol for two input pulse shapes  $\psi_{\blacktriangle}$  and  $\psi_{\blacktriangleleft}$  is presented in Fig. 2b. First, a temporal phase modulation with  $\delta(t) = \alpha|t|$ , corresponding to  $z \rightarrow z' = z - \alpha|k_z|$  transformation in the phase space implements the time-dependent-transmission beamsplitter and simultaneously performs the time-inversion of the first part. The Wigner function maps (dark background) illustrate that the two parts of the pulse after the mapping procedure are lying symmetrically on the opposite sides of the  $k_z$  space. For practical reasons the part of the pulse around  $t = 0$  is not mapped onto the atoms, but as we show in the Methods section the information is contained mostly in the tails. Finally, by performing  $k_z$ -direction splitting transformation in the phase space we overlap the two parts and make them interfere. This is achieved by imprinting a  $\pi$ -depth square-wave grating with linearly increasing grating wavevector  $k_g = \kappa z$  (see inset in Fig. 1b). The chirped grating transfers the spin wave into diffraction orders with  $z$ -dependent wavevector spacing  $k_z \rightarrow k'_z = k_z \pm \kappa z$ . To overlap the two signal pulse components at  $k_z = 0$  coordinate (the symmetry axis of the quasiprobability distribution) the grating chirp parameter  $\kappa$  has to match the storage chirp  $\kappa = 1/\alpha$ . The third row of Fig. 2 represents the Wigner function after application of the grating. By taking a  $z$ -direction integral of the quasiprobability we retrieve light intensity

at the output of the memory. We are interested in coherence components around  $k_z = 0$  that correspond to the anti-symmetric port of the interferometer. We clearly see that in the case of  $\mathcal{HG}_0$  (symmetric) input shape the interference at  $k_z = 0$  is destructive, while for  $\mathcal{HG}_1$  (antisymmetric) input shape it becomes constructive. To access the symmetric port the coherence is modulated again with similar square-wave grating, but with doubled chirp parameter  $k_g = 2\kappa z = \frac{2}{\alpha}z$ , and shifted in phase by  $\pi/2$ . This is illustrated in the fifth row of Fig. 2, where we observe constructive interference for the symmetric input shape, and destructive for anti-symmetric one. Finally, the area around  $k_z = 0$  is remapped to light which constitutes the output from the symmetric port of the interferometer (last row of Fig. 2). Notably, the interference in fact happens in the Fourier domain, as the protocol realizes a  $\pi/2$  ( $-\pi/2$ ) rotation of the Wigner function of the first (second) half of the signal pulse, corresponding to the forward (backward) Fourier transform. Therefore longer signal pulses give shorter pulses at the output of the interferometer that leads to higher signal-to-noise ratio when using noisy detectors. This provides an additional practical advantage while dealing with very narrowband states of light.

### Information in spectral resolution

Let us now introduce the theoretical framework to evaluate the super-resolution enhancement. In the conventional approach a spectrometer that measures the normalized spectral intensity  $\tilde{I}(\omega) = \frac{1}{2} (|\tilde{\psi}(\omega - \delta\omega/2)|^2 + |\tilde{\psi}(\omega + \delta\omega/2)|^2)$  is used to collect data that is then processed to estimate  $\delta\omega$  by fitting the theoretical curve. Similarly, a Fourier spectrometer measures the second-order autocorrelation, which is then Fourier-transformed to yield  $\tilde{I}(\omega)$  as well. However, this scenario, that is an analogy for real space direct imaging (DI) of two incoherent sources has been found to be not optimal [16]. This follows from a fact that DI suffers from so-called Rayleigh curse which manifests as rapid decrease of Fisher information (FI). The Cramér-Rao bound limits achievable precision for any locally unbiased estimator of the normalized separation  $\hat{\varepsilon}$  [42]:

$$\Delta^2 \hat{\varepsilon} \geq \frac{1}{N \mathcal{F}_\varepsilon}, \mathcal{F}_\varepsilon = \int \frac{1}{p_\varepsilon(x)} \left( \frac{\partial}{\partial \varepsilon} p_\varepsilon(x) \right)^2 dx, \quad (2)$$

where  $\Delta^2 \hat{\varepsilon}$  is the variance of the estimator,  $\mathcal{F}_\varepsilon$  is the Fisher information,  $N$  is the number of independent single photons used, and  $p_\varepsilon(x)$  represents the measurement outcome distribution parameterized by the true separation value  $\varepsilon$ . For Gaussian envelopes

$$\tilde{\psi}_{\blacktriangle}(\omega) = \left( \sqrt{2\pi}\sigma \right)^{-1/2} \exp \left( -\frac{\omega^2}{4\sigma^2} \right) \quad (3)$$

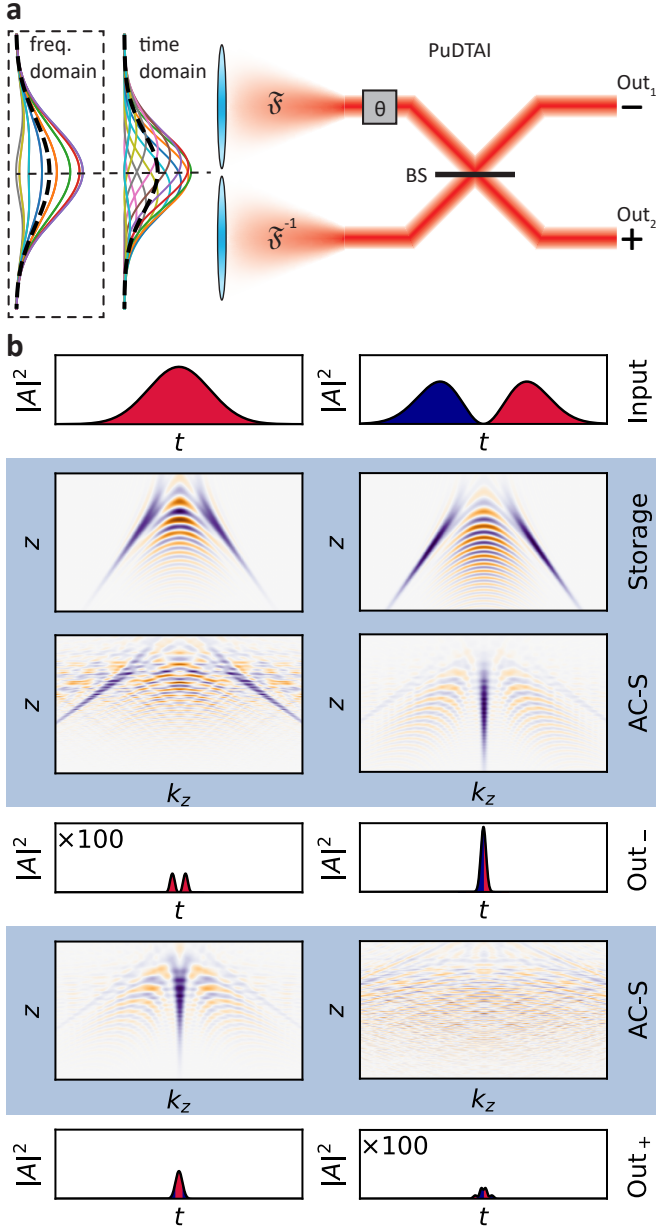


FIG. 2. **Step-by-step realization of the protocol for symmetric and anti-symmetric input signals.** **a** Schematic representation of the PuDTAI interferometer superimposing the divided signal in the Fourier space. **b** The corresponding spin-wave evolution in  $(z, k_z)$  space is represented by Wigner function maps. Thanks to the symmetrically-chirped control field used in GEM protocol (Storage) the two halves of the signal pulse are mapped in a symmetric manner on separate Fourier ( $k_z$ ) components while overlapping in the longitudinal coordinate  $z$ . The spatially-resolved AC-Stark phase modulation (AC-S) with chirped square grating splits the spin-waves in the  $k_z$  direction and makes the two half to interfere at central  $k_z$  coordinate - the anti-symmetric port of the interferometer which is then read-out by control field pulse (Out<sub>-</sub>). The second (symmetric) port is restored by modulating the spin waves again with a second chirped square wave grating with opposite phase (AC-S). The symmetric port is finally retrieved (Out<sub>+</sub>).

the Fisher information for DI in case of small separations  $\varepsilon \ll 1$  can be approximated as  $\mathcal{F}_{\text{DI}} \approx \varepsilon^2/8$ . At the same time the quantum Fisher information (QFI) [43] that places a measurement strategy independent precision bound for given estimation task turns out to have constant value  $\mathcal{F}_Q = 1/4$ . This observation has led to extensive search for different measurement schemes that will approach the ultimate bound placed by Q-CRB and will not suffer from Rayleigh curse. Most of those super-resolution measurement schemes are based on the following observation: a shifted Gaussian mode function  $\tilde{\psi}_{\Delta}(\omega \pm \delta\omega/2)$  for  $\varepsilon \ll 1$  can be approximated as an unshifted component  $\tilde{\psi}_{\Delta}(\omega)$  with a small correction of the first Hermite-Gaussian function:

$$\tilde{\psi}_{\Delta}(\omega \pm \varepsilon\sigma/2) \approx \tilde{\psi}_{\Delta}(\omega) \pm \frac{\varepsilon}{4} \tilde{\psi}_{\Delta}(\omega) \quad (4)$$

$$\tilde{\psi}_{\Delta}(\omega) = \frac{\omega}{\sigma} \left( \sqrt{2\pi}\sigma \right)^{-1/2} \exp\left(-\frac{\omega^2}{4\sigma^2}\right). \quad (5)$$

From this we see that only the anti-symmetric component  $\tilde{\psi}_{\Delta}(\omega)$ , like in the SLIVER protocol, carries the information about the separation, thus filtering out the (orthogonal) symmetric mode  $\tilde{\psi}_{\Delta}(\omega)$  leads to massive improvement of signal-to-noise ratio and boosts up the separation estimation precision. From the theoretical point of view the PuDTAI protocol presented here is a version of the SLIVER methods translated into the spectral domain. The Fisher information associated with photon detection probabilities in the symmetric  $\mathcal{P}_{\Delta}$  and anti-symmetric  $\mathcal{P}_{\Delta}$  ports exhibits extraordinary sensitivity for small ( $\varepsilon \ll 1$ ) separation estimation  $\mathcal{F}_{\text{SLIVER}} \approx \frac{1}{4} - \frac{\varepsilon^2}{32}$  and for  $\varepsilon \rightarrow 0$  approaches  $\mathcal{F}_Q$ . This framework assumes prior knowledge of the mean frequency, also known as the source centroid. This assumption is practically valid, as an adaptive strategy can be used where the centroid is first estimated with desired precision using direct detection [44].

## Experimental Results

To benchmark our protocol we artificially prepare signal pulses composed of two mutually incoherent spectral components

$$\tilde{\mathcal{S}}_{\varphi}(\omega) = \frac{1}{\sqrt{2}} \left( \tilde{\psi}_{\Delta}(\omega - \sigma\varepsilon/2) + e^{i\varphi} \tilde{\psi}_{\Delta}(\omega + \sigma\varepsilon/2) \right) \quad (6)$$

where the random phase  $\varphi \in [0, 2\pi[$  is drawn from uniform distribution. The corresponding chronocyclic Wigner function [38] of such signal distribution reads:

$$\mathcal{W}_{\mathcal{S}}(t, \omega) = \psi_{\Delta}^2(t) (\tilde{\psi}_{\Delta}^2(\omega - \sigma\varepsilon/2) + \tilde{\psi}_{\Delta}^2(\omega + \sigma\varepsilon/2))$$

We send the pulses to the memory where they are processed by our pulse-division time-inversion interferometer. To read-out the contributions in



symmetric and anti-symmetric ports we use two sequentially applied pulses of the control field that are interleaved with the second AC-Stark modulation. The processed signal light coming from the memory is detected using single-photon counting module (SPCM) and photo-counts are time-tagged to identify the output ports (see Fig. 9 for the time-bin histogram). The mean single-shot signal contribution summed over the symmetric and anti-symmetric port was set to be around  $\bar{n} \approx 0.69$ . After many experimental repetitions we count the total contributions  $N_-$ ,  $N_+$  in the anti-symmetric and symmetric port respectively and calibrate the maximum-likelihood estimator  $\hat{\varepsilon}(N_-/N_+)$  based on theoretically expected counts ratio  $N_-/N_+$ . The estimator is then used to estimate the value of the separation  $\varepsilon$ . The variance of the estimator is estimated by a bootstrapping technique. For this, from collected counts (approx.  $1.5 \times 10^5$  total counts for each separation  $\varepsilon$  setting) we randomly prepare  $10^3$  sets of samples, each containing  $1.5 \times 10^5$  total counts. The estimator is then evaluated on each set and the mean and variance of  $\hat{\varepsilon}$  is calculated. In Fig. 3a we show raw estimation results for PuDTAI protocol and DI approach on a common  $\langle \hat{\varepsilon} \rangle$  plot. The filled regions corresponds to the estimation uncertainty given by the square root of the estimator variance and normalized to 10 processed photons.

The measurements in DI scheme are obtained by using ultranarrowband far-field temporal imaging technique which we call quantum-memory temporal imaging (QMTI) [35]. The protocol employs the same GEM device. In this technique a  $90^\circ$  rotation of the signal pulse Wigner space is performed, resulting in spectrum-to-time mapping  $\omega \rightarrow 2\alpha_{\text{DI}}t$ , where  $\alpha_{\text{DI}}$  is the control field chirp parameter corresponding to the time-lens magnitude. The output signal is detected using the same SPCM as in the case of PuDTAI, where counts corresponding to distinct spectral components have different arrival time (timetags). The counts distributions with already calibrated frequency labels are presented in Fig. 3d. From those, we estimate the separation using maximum-likelihood separation estimator  $\hat{\varepsilon}_{\text{DI}}$ . The variance of this estimator is calculated by following the same bootstrapping technique as in the case of PuDTAI protocol. Figure 3b portrays the estimators' biases  $\langle \hat{\varepsilon} \rangle - \varepsilon$  proving unbiasedness of both estimators even for small  $\varepsilon$  and validating the results for variances.

In Fig. 3c we compare the achieved precision with CRB for both schemes. Here we also show the ultimate bound placed by the QFI ( $\mathcal{F}_{\text{Q}}$ ) as well as bounds for ideal SLIVER protocol ( $\mathcal{F}_{\text{SLIVER}}$ ) and noiseless DI ( $\mathcal{F}_{\text{DI}}$ ). The real bounds are placed by FIs that take into account experimental imperfection such as detection noise and finite bandwidth of the ensemble -  $\mathcal{F}_{\text{QMTI}}$ , as well as finite interferometer visibility and interferometer losses in the case of PuDTAI protocol -  $\mathcal{F}_{\text{PuDTAI}}$  (see Methods). We see that the PuDTAI protocol vastly outperforms the

QMTI for normalized separations  $\varepsilon < 1$  with maximum improvement in terms of variance of 30 for  $\varepsilon = 0.4$ . Finally, we show the data used for estimation, to better illustrate the origin of sensitivity enhancement. In Fig. 3d the results of direct imaging are presented, and we observe that for  $\varepsilon < 1$  the shape of the obtained spectrum remains close to a Gaussian. On the other hand, in Fig. 3e we show total contributions to the anti-symmetric ( $N_-$ ) and symmetric ( $N_+$ ) ports, as well as the ratio  $N_-/N_+$  along with fitted model that is used to estimate the  $\varepsilon$  without a direct need to know total source brightness.

## Discussion

We have demonstrated frequency-separation estimation which outperforms direct spectroscopy. The protocol operates in a previously unexplored regime of very narrowband light, which merits further discussion and comparison with other possible schemes. In Fig. 4 we compare several different approaches to measure frequency difference of two sources. We characterize the gain achieved with our method via the super-resolution parameter  $\mathfrak{s}$  that is interpreted as a reduction of resources (photons) required to achieved the same resolution as direct imaging spectroscopy with the same aperture  $\sigma$ . The  $\mathfrak{s}$  for a given measurement scheme characterized by the FI  $\mathcal{F}$  is calculated as  $\mathfrak{s} = \lim_{\varepsilon \rightarrow 0} (\mathcal{F}/\mathcal{F}_{\text{DI}})$ . All the conventional methods that include: grating and Fourier transform (FT) spectrometers along with far-field temporal imaging or inherently lossy scanning methods that employ cavity or EIT media fall into DI description and thus suffer from Rayleigh's curse ( $\mathfrak{s} = 1$ ). Surprisingly, there is only one more demonstration (Quantum Pulse Gate - QPG [24]) improvement over the conventional DI approach. So far, the QPG approach, that in principle enables temporal-mode demultiplexing, allowed projecting only a single mode at a time. In our work we are able to observe two modes (ports) in the same experiment. An important future challenge in both cases is to allow truly multi-mode sorting.

While using DI (a spectrometer) for high bandwidth signals seems an obvious choice, one may conclude that for narrowband signals a balanced heterodyne (or homodyne) detection would perform better. The first obvious challenge is that one then needs a stable and narrowband local oscillator, but as our method uses a control field, this requirement is effectively shared. However, when the sources brightness is low (below one photon per mode), the heterodyne detection scheme suffers strongly from shot noise. For the particular task of separation estimation, the shot noise will spoil the estimation precision and makes it useless for measuring

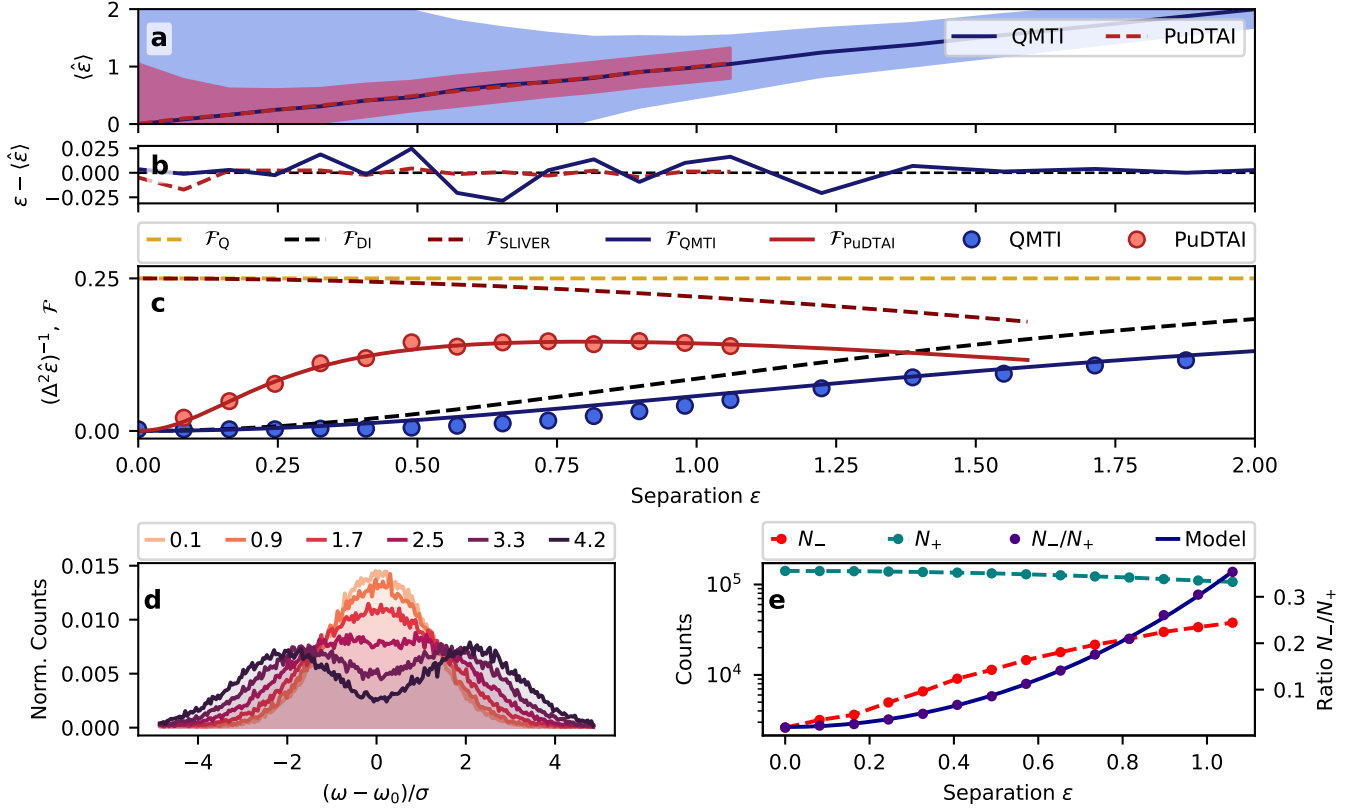


FIG. 3. **Separation estimation using QMTI and PuDTAI protocols.** **a** Raw  $\varepsilon$  estimates obtained from DI approach (QMTI) and PuDTAI protocol. The shaded regions represent estimation uncertainty given by the square root of the estimator variance (SEM) normalized for 10 processed photons. **b** Estimator's biases for both schemes. **c** Estimation precision compared with idealized and real world CRBs given by corresponding Fisher information ( $\mathcal{F}_Q$ - Quantum Fisher information,  $\mathcal{F}_{\text{SLIVER}}$  - ideal SLIVER protocol,  $\mathcal{F}_{\text{DI}}$  - ideal DI spectrometer,  $\mathcal{F}_{\text{QMTI}}$  - Quantum memory temporal imaging,  $\mathcal{F}_{\text{PuDTAI}}$  - PuDTAI protocol). **d** Frequency-labeled single photon counts distributions obtained with QMTI spectrometer for different true separation values  $\varepsilon$ . **e** Contributions to the anti-symmetric ( $N_-$ ) and symmetric ( $N_+$ ) port of the PuDTAI device and the ratio  $N_-/N_+$  along with calibrated theoretical model.

single-photon-level sources. Nevertheless, heterodyne (or homodyne) can overcome the Rayleigh curse for higher signal photon levels and for small separations as has been recently analyzed in detail for the spatial domain [45] ( $\xi > 1$  for average 7.2 photons per mode and more), with the use of optimized data analysis, as opposed to simply looking at power spectral densities. Therefore, a purely photon-counting method is in general needed in the low light-level regime.

We envisage that other platform may be used to implement the protocol we proposed, also in different frequency regimes. For example, rare-earth doped crystals such as  $\text{Eu:Y}_2\text{SiO}_5$  offer narrow homogeneous absorption linewidth that can be dynamically broadened with an electric field [46] for the purpose of time-frequency domain multimode storage [47]. Processing with AC-Stark shifts has also been demonstrated [48], and advances in embedding ions in waveguides promise good efficiency and noise properties.

Another approach has been very recently discussed

theoretically by *Shah and Fan* [49], who considered a transformation device based on pulse shapers and electro-optic modulators. This approach may be very applicable where relevant devices can operate, which is in particular GHz-bandwidth regime in the telecom band of light. In this regime no quantum memory is required, as the timescales involved are much shorter. Several other quantum-information protocols have been realized with similar means, also for quantum light, and the scheme is generally termed quantum-frequency processor [50].

Remarkably, the PuDTAI protocol has been realized here in a quantum memory that insensitive to the signal spatial distribution. This means that it can accept external fluorescence light that is in principle spatially-multimode. Furthermore, we note that to analyze fluorescent light from different kinds of samples, one needs to match the wavelength of operation. This can be done via the maturing techniques of quantum frequency conversion [51].

The path from resolving two sources to obtaining a

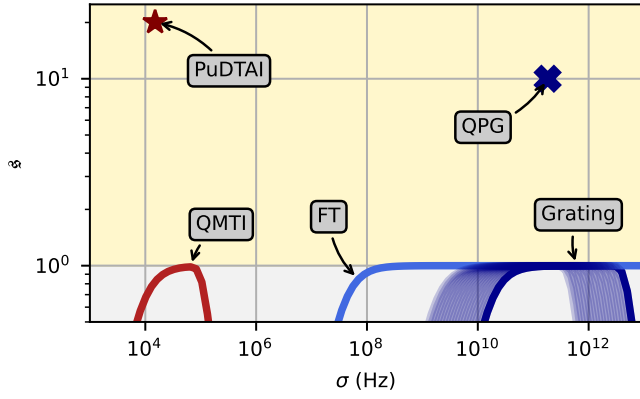


FIG. 4. **Comparison of super-resolution enhancement factor  $\zeta$  of different spectrometers and super-resolution spectroscopy techniques.** All conventional methods (Grating, FTS - Fourier transform spectrometer) and the temporal-imaging method using our quantum memory (QMTI - quantum-memory temporal imaging) are analogous to the DI approach and thus are limited by the Rayleigh curse. Only two (QPG - Quantum Pulse Gate [24] and PuDTAI - *this work*) beat the limit of  $\zeta = 1$  and thus achieve super-resolution. The curves represent exemplary realizations of given spectrometer realizations for constant time-bandwidth product.

more complex spectrum with super-resolved features is challenging, yet some knowledge can be drawn from imaging problems considered so far. Various groups have considered the cases of three sources in two dimensions [52, 53], or two sources with arbitrary brightness [54], and practical frameworks for multi-pixel images are being developed as well [55]. For the spectroscopic case discussed here, different operations in the quantum memory will be needed to prepare measurements optimal for multi-source scenarios.

## METHODS

### Gradient Echo Memory

The Gradient Echo Memory is based on pencil-shaped ( $8 \times 0.3 \times 0.3 \text{ mm}^3$ )  $^{87}\text{Rb}$  atomic cloud prepared in magneto-optical trap. The experimental sequence is depicted in Fig. 5 After the cloud preparation stage (trapping, compression and cooling) the atoms are optically pumped to the  $|h\rangle = (F = 2, m_F = -2)$  state. The control field (795 nm) couples the excited state  $|e\rangle = (F = 1, m_F = -1)$  with the previously emptied storage state  $|g\rangle = (F = 1, m_F = 0)$  which enables coherent absorption of the signal field at the  $|h\rangle \rightarrow |e\rangle$  transition. The magnetic field gradient crucial to the GEM protocol is generated by two identical coils located anti-symmetrically on the  $z$ -axis and powered by fast H-topology current switch, that allows switching

between negative and positive gradients within  $5 \mu\text{s}$ . In the experiment we set the gradient to  $\pm 7.3 \mu\text{T/mm}$ . Additionally, to separate the magnetically broadened absorption spectrum of the  $|h\rangle \rightarrow |e\rangle \rightarrow |g\rangle$  transition from the unbroadened clock transition ( $F = 2, m_F = -1 \rightarrow (F = 1, m_F = 0) \rightarrow (F = 1, m_F = 1)$ ) we keep the cloud in constant magnetic field of  $120 \mu\text{T}$  magnitude along the  $z$ -axis. Moreover, to stabilize the two photon detuning that is sensitive to magnetic fields we operate the protocol at 50 Hz synced with local mains frequency and correct for slow magnetic fluctuations (caused for example by elevator near our laboratory) by adjusting the magnitude of the constant magnetic field in a feedback scheme described below.

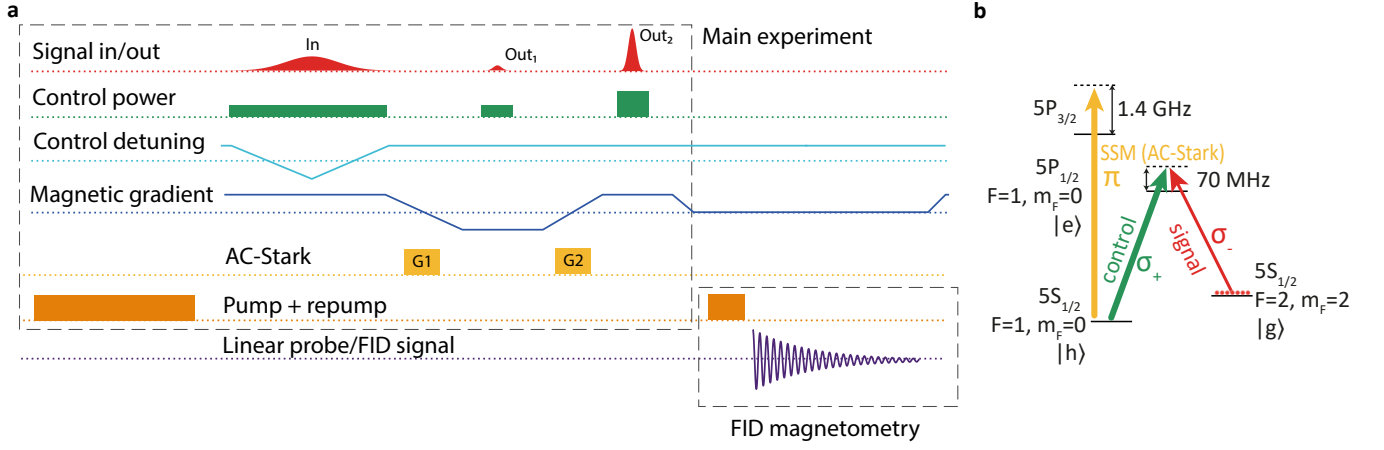
The signal photons are passed through an optically-pump  $^{87}\text{Rb}$ -vapour cell in order to remove the residual control field. At the end, they are coupled to a single-mode fiber and detected with an SPCM.

### Magnetic field synchronization and stabilization

The protocol operates at 50 Hz repetition rate synced with local mains frequency. The synchronization mechanism is realized by the FPGA (NI 7852R) system controlling the whole sequence. The synchronization (waiting for mains trigger) happens during the trapping period of each experimental repetition effectively providing no-idle-time operation. The slow (below 50 Hz) magnetic field fluctuations are compensated by feedback mechanism that is enabled at the end of each sequence repetition. This is achieved by repumping the atoms to the  $m_F = -2$  sublevel, switching off the GEM gradient and probing the atomic spin precession with linearly polarized probe beam at  $(F = 2) \rightarrow (F = 1)$  transition illuminating the whole ensemble from the side. The polarization-rotation signal is registered by differential photodiode and the precession frequency is estimated in real time by fitting a quadratic function around the maximum of registered signal Fourier spectrum. From this, the frequency-error signal is obtained and fed to PI controller that modulates the current in the  $z$ -direction compensation coils (see Fig. 1 for reference). With the compensation mechanism active, we achieve long-term rms stability of 130 Hz of the Larmor frequency, corresponding to 18.5 nT. This translates to the stability of the relative frequency centroid of twice the Larmor frequency, i.e. 260 Hz, which is well below the desired resolution.

### Signal pulse preparation

The signal and control pulses are carved out from two branches of a continuous wave frequency-stabilized [56] laser. The first branch, used for signal pulse generation



is derived by frequency-shifting by 6834 MHz part of laser light using EOM and Fabry-Pérot filtering cavity (see [39] for details). Then the signal pulses are carved with double-pass AOMs feed by home-made arbitrary waveform generator consisting of *Red Pitaya* running the *PyRPL* [57] software and external frequency mixer providing upconversion of the carrier frequency to the desired 80 MHz. The setup is depicted in Fig. 6. The *Red Pitaya* with *PyRPL* allows us to prepare arbitrary (up to bandwidth limitations of 50 MHz) complex envelopes that are internally multiplied by the carrier waveform at 35 MHz using digital IQ mixer. The signal is then externally mixed with 45 MHz local oscillator from Direct Digital Synthesizer controlled by the main FPGA system to match the AOM central frequency of 80 MHz and provide extended amplitude dynamic range.

The frequency-domain double-Gaussian signal  $\tilde{S}_\varphi(\omega)$  is generated by programming a temporal envelope  $S_\varphi(t) = S \cos(\frac{\delta\omega t - \varphi}{2}) \exp(-t^2\sigma^2)$  with given  $\delta\omega = \sigma\varepsilon$ . During the measurements, to make the virtual sources mutually incoherent we continuously ( $\bmod 2\pi$ ) change the phase  $\varphi$  from  $-\pi$  to  $\pi$  in a way that for single measurement the number of complete  $2\pi$  cycles is in order of few thousands.

#### *PuDTAI Model and calibrations*

The schematic representation of the theoretical model is depicted in Fig. 7. The model follows image-inversion interferometer description with two mutually incoherent weak ( $\bar{n} \ll 1$ ) sources at the input.

By design, our interferometer superimposes the two

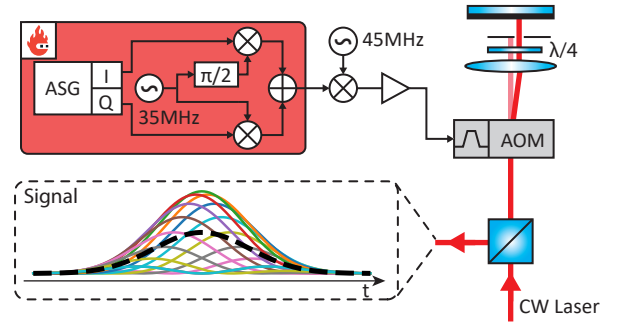


FIG. 6. **Experimental setup used to generate frequency-domain double-Gaussian signal  $\tilde{S}_\varphi(\omega)$ .** The in-phase (I) and quadrature (Q) signal components are mixed with intermediate carrier frequency at 35 MHz using digital IQ-mixer. The resulting radio-frequency (RF) signal is then up-converted by 45 MHz with help of analog mixer. Finally, the RF signal with carrier frequency at 80 MHz is feed into acousto-optic modulator in double pass configuration that carves the light pulses from continuous wave laser.

arms in the Fourier space. This can be most easily understood by investigating the Wigner function transformations of the two signal pulse halves during propagation through the interferometer. Let us focus on the first half that has a temporal amplitude:

$$\mathcal{A}_-(t) = \begin{cases} \mathcal{A}(t) & t < 0 \\ 0 & t \geq 0 \end{cases}. \quad (7)$$

The time-dependent two photon detuning which for  $t < 0$  is  $\delta(t) = \alpha t$  virtually applies a temporal phase profile  $\mathcal{A}_-(t) \rightarrow \mathcal{A}_-(t) \exp(i\frac{\alpha}{2}t^2)$  that corresponds to  $z \rightarrow$



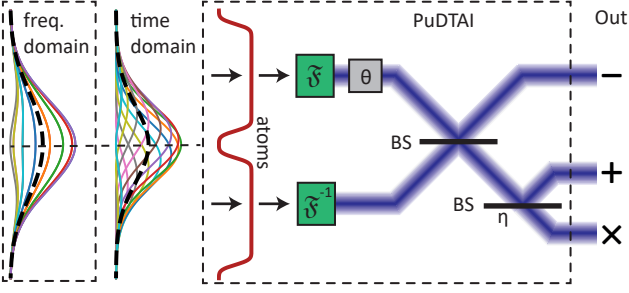


FIG. 7. **Schematic representation of PuDTAI model.**

The input signal passes through temporal aperture and is split into two halves. The upper and lower parts are Fourier transformed ( $\mathcal{F}$ ) (inverse transform -  $\mathcal{F}^{-1}$  - for the lower part) and combined on the beamsplitter (BS) with relative phase set to  $\theta$ . The first output port ( $\text{Out}_-$ ) is directly detected while the second port ( $\text{Out}_+$ ) before detection experiences additional loss due to lossy (maximally 82% efficiency) implementation of the first beamsplitter.

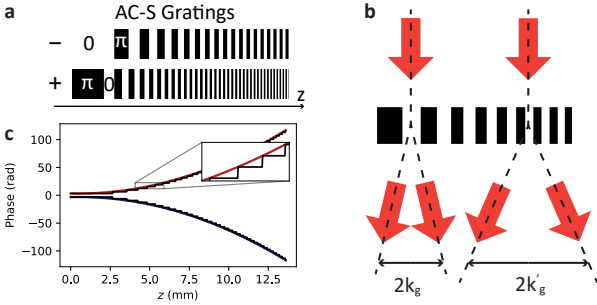


FIG. 8. Chirped square-wave phase grating used to simultaneously apply positive and negative quadratic phase in space. a - Two gratings used to implement the anti-symmetric (-) and symmetric (+) PuDTAI ports. b The coherence at longitudinal positions  $z$  is split into diffraction orders that are separated by the grating local wavevector  $k_g = \kappa z$ . c Interpretation of the chirped square-wave grating as a superposition of positive and negative quadratic Fresnel phase profiles.

$z' = z - \alpha k_z$  transformation of the associated atomic coherence Wigner function  $\mathcal{W}_-(z, k_z)$ . In the language of temporal imaging this operation is known as propagation through temporal lens with the focal length  $f_t = \omega_0/\alpha$  [35] where  $\omega_0$  is the optical carrier frequency. The SSM modulation with spatially chirped square grating with wavevector  $k_g = \kappa z$  splits the coherence into multiple diffraction orders. However, as the depth of the grating is  $\pi$  the 0-th diffraction order vanishes and the coherence is mostly split to  $\pm 1$  orders (ideally, only 18% is distributed into higher orders). In the case of the first half of the signal pulse we are interested in the  $-1$ -st order, that when isolated can be understood as a result of quadratic phase modulation in the real space:  $\varrho_{hg}(z) \rightarrow \varrho(z) \exp(i\frac{\kappa}{2}z^2)$ . This corresponds to the  $k_z \rightarrow k'_z = k_z \pm \kappa z$  transformation of the Wigner function

$\mathcal{W}_-(z, k_z)$  and in terms of temporal imaging represents temporal propagation by a distance  $d_t = \kappa/\omega_0\beta^2$  where  $\beta$  is the Zeeman shift gradient slope that facilitates the spectrum-to-space mapping. With  $\kappa = 1/\alpha$  that means  $d_t = f_t$  the full transformation reads:

$$k_z \rightarrow k'_z = \kappa z \quad (8)$$

$$z \rightarrow z' = z - \frac{1}{\kappa}k_z \quad (9)$$

which up to the additional temporal phase modulation represents a counter-clockwise  $90^\circ$  rotation of the phase space, that in fact is a backward Fourier transform. Similarly for the second half of the pulse (for  $t \geq 0$ ), as the sign of  $\alpha$  changes we get a clockwise rotation and thus forward Fourier transform. Finally, as at the input we have the full signal pulse  $\mathcal{A}(t) = \mathcal{A}_-(t) + \mathcal{A}_+(t)$  the two components interfere in the Fourier domain when the positive frequency components of the first half are superimposed onto the negative components of the second half thus implementing the inversion interferometer. Additionally, the by design Fourier transform feature of our PuDTAI interferometer can improve the signal-to-noise ratio when using noisy detectors as long signal pulses result in short pulses at the interferometer output.

With the separation parameter  $\varepsilon = \delta\omega/\sigma$  and temporal representation of the input signal given by:

$$\mathcal{S}_\varphi(t) = \psi_\Delta(t) \sqrt{2} \cos\left(\frac{\delta\omega t - \varphi}{2}\right) \exp\left(\frac{i\varphi}{2}\right) \quad (10)$$

that at the interferometer input is clipped by the (symmetric) temporal aperture function  $f_\Delta(t)$ , we may write the following amplitudes for the anti-symmetric and symmetric ports:

$$u_-(t) = \frac{1}{2} \sqrt{\eta} f_\Delta(t) (\mathcal{S}_\varphi(t) - \mathcal{S}_\varphi(-t)), \quad (11)$$

$$u_+(t) = \frac{1}{2} \sqrt{\eta} f_\Delta(t) (\mathcal{S}_\varphi(t) + \mathcal{S}_\varphi(-t)), \quad (12)$$

where we introduced also the mean efficiency  $\eta$ . As the interferometer internally performs a Fourier transform of the input signal, at the device output we observe the counts distributions given by these two components in the frequency domain  $\tilde{p}_i(\omega) = |\tilde{u}_i(\omega)|^2$  (see Fig. 9 for example of measured counts distributions, with  $\omega = \alpha t$ ).

The total contributions in the anti-symmetric and symmetric ports are calculated as  $p_i = \int \tilde{p}_i(\omega) d\omega$  which corresponds to using a spectral bucket (no frequency information) detector. After introducing non-perfect interference visibilities  $\mathcal{V}_-$  and  $\mathcal{V}_+$  and additional losses in the symmetric port  $\eta_+$  we arrive at outcome probabilities that for hard aperture function given by

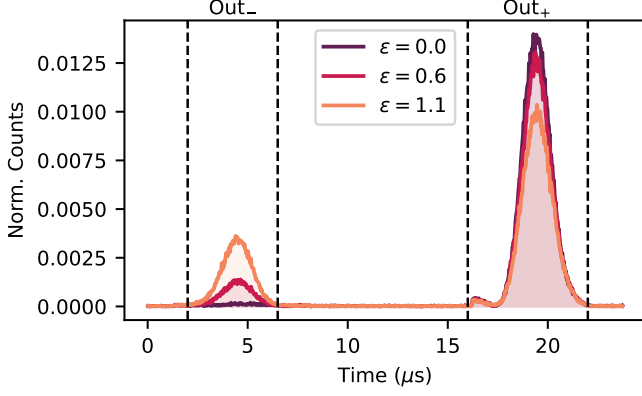


FIG. 9. **Time-bin outputs of the spin-wave interferometer.** Single-photon counts distributions registered at each port of the PuDTAI interferometer for several chosen true separation values  $\varepsilon$ .

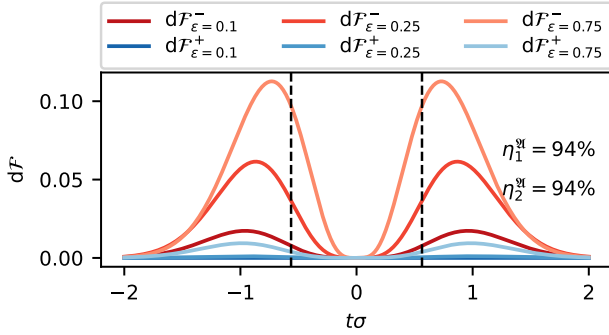


FIG. 10. **Fisher information density  $d\mathcal{F}_\varepsilon$  for direct detection of the anti-symmetric (-) and symmetric (+) subspace with the realistic parameters  $\mathcal{V}_-$  and  $\mathcal{V}_+$ .** For small  $\varepsilon$  the information is concentrated in the two lobes outside the central part of the spectrum. The relative efficiencies  $\eta_1^A$ ,  $\eta_2^A$  correspond to the hard aperture (marked as dashed lines) that removes the input signal located within the  $t\sigma \pm 0.564$  range.

$f_A(t) = \Theta(-t_A - t) + \Theta(-t_A + t)$  take the form:

$$p_- = \frac{\eta}{2} \left( \text{erfc}(\sqrt{2}\sigma t_A) - \mathcal{V}_- e^{-\frac{\varepsilon^2}{8}} f(t_A, \varepsilon) \right), \quad (13)$$

$$p_+ = \frac{\eta\eta_+}{2} \left( \text{erfc}(\sqrt{2}\sigma t_A) + \mathcal{V}_+ e^{-\frac{\varepsilon^2}{8}} f(t_A, \varepsilon) \right), \quad (14)$$

$$p_\times = 1 - p_- - p_+, \quad (15)$$

where  $f(t_A, \varepsilon) = \frac{1}{2} \left( \text{erfc} \left( \frac{4t_A\sigma - i\varepsilon}{2\sqrt{2}} \right) + \text{erfc} \left( \frac{4t_A\sigma + i\varepsilon}{2\sqrt{2}} \right) \right)$ . The  $p_-$ ,  $p_+$  are probabilities of detecting photon in the anti-symmetric and symmetric interferometer port respectively, while  $p_\times$  is a probability of no detection event.

The atomic cloud size along with the strength of the magnetic field gradient and slope of the control field chirp

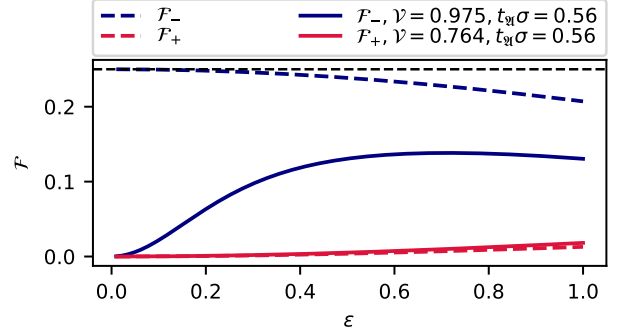


FIG. 11. **Fisher information available at each output port of the PuDTA device.** For small separations  $\varepsilon \ll 1$  the anti-symmetric port ( $\mathcal{F}_-$  corresponding to  $p_-$ ) contains most information about  $\varepsilon$ . The dashed lines represents the ideal case of  $\mathcal{V}_\pm = 1$  and infinite aperture.

$\alpha$  limits the temporal aperture  $A$  of the interferometer. We design the aperture to contain most informationally valuable parts of input signal while at the same reducing the impact of the instantaneous control chirp reversal at  $t = 0$ . This reversal by being inherently broadband spoils the time-to-position mapping by virtually locally broadening the input signal. To get rid of this effect we chose the central two photon detuning  $\delta(t = 0)$  to be outside the magnetically broadened absorption spectrum providing no light-to-atoms mapping at the  $\alpha$  reversal time. This forms an Cassegrain type aperture described by  $f_A$  that limits mostly the efficiency in the second interferometer port, that for  $\varepsilon \ll 1$  contains no information, and serves only as brightness reference for the first port. We show this in Fig 11, where we plot the Fisher information densities defined as:

$$d\mathcal{F}_i = \frac{1}{p_i(t)} \left( \frac{\partial}{\partial \varepsilon} p_i(t) \right)^2 dt. \quad (16)$$

The impact of the aperture on photon flux efficiencies in the symmetric and anti-symmetric port can be investigated by comparing the photon detection probabilities (Eq. 13 and Eq. 14) with the case of infinite aperture  $t_A = 0$  and taking the limit of  $\varepsilon \rightarrow 0$ . This gives  $\eta_{p_-}^A \approx \text{erfc}(\sqrt{2}\sigma t_A) + 2\sqrt{2/\pi}\sigma t_A \exp(-2\sigma^2 t_A^2)$  and  $\eta_{p_+}^A \approx \text{erfc}(\sqrt{2}\sigma t_A)$  which for realistic aperture  $t_A = 0.564/\sigma$  gives  $\eta_{p_-}^A \approx 0.74$ ,  $\eta_{p_+}^A \approx 0.26$ . However, in the context of  $\varepsilon$  estimation those are not crucial, and we should look how the FI changes with the  $t_A$ . The FI density 16 integrated over the aperture gives the total FI available at the outputs of the device  $\mathcal{F}_i^A = \int_A d\mathcal{F}_i$  that can be utilized when using a spectrally-resolved detection. Notably, in the case of infinite aperture and ideal visibility the total FI at the output  $\mathcal{F}_\Sigma^\infty = \mathcal{F}_-^\infty + \mathcal{F}_+^\infty$  is independent of  $\varepsilon$  and equals QFI which

means that shapes of the distributions at each port of the device contain additional information that can improve the resolution for larger  $\varepsilon$  values as has been previously recognized in the context of real-space imaging [22]. To investigate the impact of the finite aperture  $\mathfrak{A}$  we calculate the FI  $\mathcal{F}_{\pm}^{\mathfrak{A}}$  and evaluate the efficiencies as  $\eta_{\mathcal{F}_{\pm}^{\mathfrak{A}}}^{\mathfrak{A}} = \mathcal{F}_{\pm}^{\mathfrak{A}}/\mathcal{F}_{\pm}^{\infty}$  which in the case of our aperture and visibilities both approximately equals 94% as included in Fig. 10. In the case of spectral bucket detector, the total Fisher information calculated for the observable outcome probabilities ((11),(12)) takes the form:

$$\mathcal{F}_{\text{PuDTAI}} = \underbrace{\frac{\eta^2 \mathcal{V}_-^2 F}{64p_-}}_{\mathcal{F}_-} + \underbrace{\frac{\eta^2 \eta_+^2 \mathcal{V}_+^2 F}{64p_+}}_{\mathcal{F}_+}, \quad (17)$$

$$F = e^{-\varepsilon^2/4} \left( \sqrt{2/\pi} e^{-2t_{\mathfrak{A}}^2 \sigma^2 + \varepsilon^2/8} \sin(t_{\mathfrak{A}} \sigma \varepsilon) + \frac{\varepsilon}{2} f(t_{\mathfrak{A}}, \varepsilon) \right), \quad (18)$$

Interestingly, when we now evaluate the FI efficiencies in the similar way as in the case of spectrally-resolved detection and with the finite visibilities we may observe improvement over the apertureless case for certain  $\varepsilon$  range. This is direct result of filtering the informationally not valuable central part of the signal that contains most of the leaking (due to  $\mathcal{V} < \infty$ ) photons. The improvement is most prominent for  $\varepsilon \rightarrow 0$  and in our case reads  $\eta_-^{\mathfrak{A}} = \eta_+^{\mathfrak{A}} \approx 2.1$ . The experimental parameters  $\mathcal{V}_- \approx (97.51 \pm 0.03)\%$ ,  $\mathcal{V}_+ = (76.4 \pm 0.8)\%$ ,  $t_{\mathfrak{A}} \sigma \approx 0.564 \pm 0.002$  and the efficiency  $\eta_+ \approx 0.719 \pm 0.009$  are obtained from calibration measurements consisting on running the protocol for different  $\varepsilon$  and interferometer phase  $\theta$ .

Finally, we can also evaluate the mean efficiencies of storage retrieval from the memory. We obtain  $\eta_1 = 0.83\%$  and  $\eta_2 = 0.60\%$ . We note that those efficiencies are very similar to the ones obtained in the QPG protocol [24]. To boost the efficiencies of the GEM one could design a larger and more dense atomic ensemble or prepare the ensemble inside a cavity resonant with the signal field that effectively boosts the optical depth and thus the efficiency [58–60].

#### Superresolution parameter

The classical (DI) spectrometers such as Grating, FT and QMTI that are not tailored to the given signal mode function  $\tilde{\psi}(\omega)$  can be directly used with signals that have different FWHM or  $\sigma$ . To indicate that these are represented as lines covering some  $\sigma$  range that depend on given spectrometer implementation. The super-resolution parameter  $\zeta$  in this case is calculated using the same formula as in the case of spectrometers tailored for the given  $\tilde{\psi}(\omega)$  such as PuDTAI or QPG. Any DI spectrometer has its bandwidth (BWL) and resolution limit (RL). These are causing the  $\mathfrak{s}$  parameter

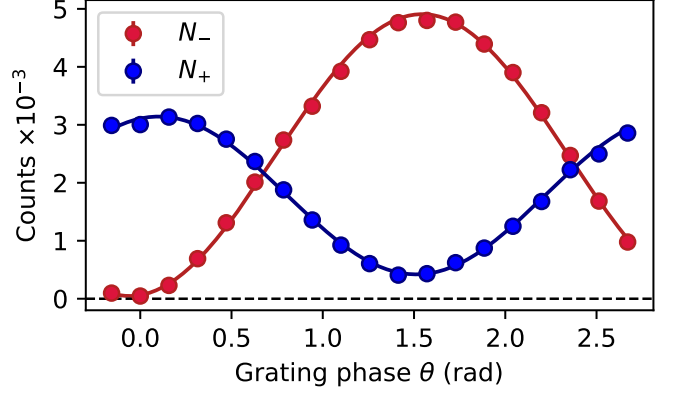


FIG. 12. **Direct demonstration of high interference visibility.** The PuDTAI interferometer phase  $\theta$  scan for fixed separation parameter  $\varepsilon = 0$  along with fitted sine and cosine functions.

to drop below 1 for signals with bandwidth exceeding the BWL or that are narrower than RL. The limitation from the finite RL broadens the signal mode function  $\tilde{\psi}(\omega)$  and thus spoils the separation estimation sensitivity by virtually making the  $\varepsilon$  smaller. For a RL given by  $\sigma_{\text{RL}}$  the broadening effect can be calculated as  $\sigma \rightarrow \sqrt{\sigma^2 + \sigma_{\text{RL}}^2}$  which result in the  $\varepsilon$  smaller by  $\frac{\sigma}{\sqrt{\sigma^2 + \sigma_{\text{RL}}^2}}$  factor. On the other hand the BWL characterized by  $\Sigma_{\text{BWL}}$  cuts the informationally valuable tails of signals with  $\sigma > \Sigma_{\text{BWL}}$  that results in drop of the Fisher information given as  $\mathcal{F}_{\text{DI}} = \int_{\Sigma_{\text{BWL}}} d\mathcal{F}_{\text{DI}}$  with the  $d\mathcal{F}_{\text{DI}}$  being the DI Fisher information density and the integration goes through the whole available bandwidth. In Fig. 4 we plot several  $\zeta$  curves for various DI spectrometers. These are: Grating - a grating spectrometer with gratings of lengths ranging from 1 cm to 10 cm, with grating period of  $1/1200 \text{ mm}^{-1}$  and  $\Sigma_{\text{BWL}} = 10^3 \times \sigma_{\text{RL}}$ ; FT - Bruker IFS 125HR Fourier transform spectrometer with  $0.001 \text{ cm}^{-1}$  resolution and  $50 \times 10^3 \text{ cm}^{-1}$  and the MIR spectral range; QMTI - the Quantum Memory Temporal Imaging Spectrometer with  $\sigma_{\text{RL}} = 7.2 \text{ kHz}$  and  $300 \text{ kHz}$  BWL.

#### DATA AVAILABILITY

The data that support the findings of this study are available from the corresponding authors upon reasonable request.

#### ACKNOWLEDGMENTS

We thank W. Wasilewski and K. Banaszek for generous support and discussions. This work has been funded by National Science Centre (Poland) grant no. 2017/25/N/ST2/00713, Ministry of Education and Science (Poland) “Diamantowy Grant” project no.

DI2016 014846, Office of Naval Research (USA) grant no. N62909-19-1-2127 and by the Foundation for Polish Science MAB/2018/4 “Quantum Optical Technologies” project. The Quantum Optical Technologies project is carried out within the International Research Agendas program of the Foundation for Polish Science co-financed by the European Union under the European Regional Development Fund. Michał Parniak was also supported by the Foundation for Polish Science via the START scholarship.

## AUTHOR CONTRIBUTIONS

M.M. and M.P. conceived the scheme and planned the experiment and the theoretical research. M.M., A.L. and M.P. contributed to the experimental setup, software and data collection. M.M. analyzed the data, developed theory and prepared figures. M.M. and M.P. wrote the manuscript. All authors discussed the results.

## COMPETING INTERESTS

The authors declare no competing interests.

---

\* [m.parniak@cent.uw.edu.pl](mailto:m.parniak@cent.uw.edu.pl)

- [1] M. Orrit, T. Ha, and V. Sandoghdar, *Chemical Society Reviews* **43**, 973 (2014).
- [2] K. B. Beć, J. Grabska, and C. W. Huck, *Analytica Chimica Acta* **1133**, 150 (2020).
- [3] C. R. Kitchin, *Optical Astronomical Spectroscopy* (Routledge & CRC Press, 1995).
- [4] J. A. Kim, D. J. Wales, and G.-Z. Yang, *Progress in Biomedical Engineering* **2**, 042001 (2020).
- [5] R. Cheng, C.-L. Zou, X. Guo, S. Wang, X. Han, and H. X. Tang, *Nature Communications* **10**, 4104 (2019).
- [6] N. Savage, *Nature Photonics* **3**, 601 (2009).
- [7] K. Hashimoto and T. Ideguchi, *Nature Communications* **9**, 4448 (2018).
- [8] A. Watanabe and H. Furukawa, *Optics Express* **26**, 27787 (2018).
- [9] U. Paudel and T. Rose, *Optics Express* **28**, 16469 (2020).
- [10] T. Dertinger, R. Colyer, G. Iyer, S. Weiss, and J. Enderlein, *Proceedings of the National Academy of Sciences of the United States of America* **106**, 22287 (2009).
- [11] M. J. Rust, M. Bates, and X. Zhuang, *Nature Methods* **3**, 793 (2006).
- [12] E. Betzig, G. H. Patterson, R. Sougrat, O. W. Lindwasser, S. Olenych, J. S. Bonifacino, M. W. Davidson, J. Lippincott-Schwartz, and H. F. Hess, *Science* **313**, 1642 (2006).
- [13] D. Gatto Monticone, K. Katamadze, P. Traina, E. Moreva, J. Forneris, I. Ruio-Berchera, P. Olivero, I. Degiovanni, G. Brida, and M. Genovese, *Physical Review Letters* **113**, 143602 (2014).
- [14] F.R.S. Lord Rayleigh, *The London, Edinburgh, and Dublin Philosophical Magazine and Journal of Science* **8**, 261 (1879).
- [15] A. Boschetti, A. Taschin, P. Bartolini, A. K. Tiwari, L. Pattelli, R. Torre, and D. S. Wiersma, *Nature Photonics* **14**, 177 (2020).
- [16] M. Tsang, R. Nair, and X.-M. Lu, *Physical Review X* **6**, 031033 (2016).
- [17] M. Tsang, *New Journal of Physics* **19**, 023054 (2017).
- [18] F. Yang, R. Nair, M. Tsang, C. Simon, and A. I. Lvovsky, *Physical Review A* **96**, 063829 (2017).
- [19] C. Lupo, Z. Huang, and P. Kok, *Physical Review Letters* **124**, 080503 (2020).
- [20] W.-K. Tham, H. Ferretti, and A. M. Steinberg, *Physical Review Letters* **118**, 070801 (2017).
- [21] R. Nair and M. Tsang, *Optics Express* **24**, 3684 (2016).
- [22] R. Nair and M. Tsang, *Physical Review Letters* **117**, 190801 (2016).
- [23] M. Paúr, B. Stoklasa, Z. Hradil, L. L. Sánchez-Soto, and J. Rehacek, *Optica* **3**, 1144 (2016).
- [24] J. Donohue, V. Ansari, J. Řeháček, Z. Hradil, B. Stoklasa, M. Paúr, L. Sánchez-Soto, and C. Silberhorn, *Physical Review Letters* **121**, 090501 (2018).
- [25] V. Ansari, B. Brecht, J. Gil-Lopez, J. M. Donohue, J. Řeháček, Z. Hradil, L. L. Sánchez-Soto, and C. Silberhorn, *PRX Quantum* **2**, 010301 (2021).
- [26] S. Zaiser, T. Rendler, I. Jakobi, T. Wolf, S.-Y. Lee, S. Wagner, V. Bergholm, T. Schulte-Herbrüggen, P. Neumann, and J. Wrachtrup, *Nature Communications* **7**, 12279 (2016).
- [27] T. Rosskopf, J. Zopes, J. M. Boss, and C. L. Degen, *npj Quantum Information* **3**, 33 (2017).
- [28] D. R. Glenn, D. B. Bucher, J. Lee, M. D. Lukin, H. Park, and R. L. Walsworth, *Nature* **555**, 351 (2018).
- [29] T. Gefen, A. Rotem, and A. Retzker, *Nature Communications* **10**, 4992 (2019).
- [30] M. Mirhosseini, A. Sipahigil, M. Kalaei, and O. Painter, *Nature* **588**, 599 (2020).
- [31] K. Wicker and R. Heintzmann, *Optics Express* **15**, 12206 (2007).
- [32] K. Wicker, S. Sindbert, and R. Heintzmann, *Optics Express* **17**, 15491 (2009).
- [33] W. Larson, N. V. Tabiryan, and B. E. A. Saleh, *Optics Express* **27**, 5685 (2019).
- [34] W. Larson and B. E. A. Saleh, *Physical Review A* **102**, 013712 (2020).
- [35] M. Mazelanik, A. Leszczyński, M. Lipka, M. Parniak, and W. Wasilewski, *Optica* **7**, 203 (2020).
- [36] Y.-W. Cho, G. T. Campbell, J. L. Everett, J. Bernu, D. B. Higginbottom, M. T. Cao, J. Geng, N. P. Robins, P. K. Lam, and B. C. Buchler, *Optica* **3**, 100 (2016).
- [37] M. Hosseini, B. M. Sparkes, G. Hétet, J. J. Longdell, P. K. Lam, and B. C. Buchler, *Nature* **461**, 241 (2009).
- [38] L. Cohen, *Time-frequency analysis*, Prentice-Hall signal processing series (Prentice Hall PTR, Englewood Cliffs, N.J., 1995).
- [39] M. Parniak, M. Mazelanik, A. Leszczyński, M. Lipka, M. Dąbrowski, and W. Wasilewski, *Physical Review Letters* **122**, 063604 (2019).
- [40] M. Mazelanik, M. Parniak, A. Leszczyński, M. Lipka, and W. Wasilewski, *npj Quantum Information* **5**, 10.1038/s41534-019-0136-0 (2019).



- [41] M. Lipka, A. Leszczyński, M. Mazelanik, M. Parniak, and W. Wasilewski, *Physical Review Applied* **11**, 034049 (2019).
- [42] S. M. Kay, *Fundamentals of Statistical Signal Processing: Estimation Theory*, edited by S. E. A. V. Oppenheim (Prentice Hall, 1993).
- [43] C. W. Helstrom, *Quantum detection and estimation theory* (Academic Press, 1976).
- [44] M. R. Grace, Z. Dutton, A. Ashok, and S. Guha, *J. Opt. Soc. Am. A* **37**, 1288 (2020).
- [45] C. Datta, M. Jarzyna, Y. L. Len, K. Łukanowski, J. Kołodyński, and K. Banaszek, *Physical Review A* **102**, 063526 (2020).
- [46] A. L. Alexander, J. J. Longdell, M. J. Sellars, and N. B. Manson, *Phys. Rev. Lett.* **96**, 043602 (2006).
- [47] A. Fossati, S. Liu, J. Karlsson, A. Ikesue, A. Tallaie, A. Ferrier, D. Serrano, and P. Goldner, *Nano Letters* **20**, 7087 (2020).
- [48] T.-S. Yang, Z.-Q. Zhou, Y.-L. Hua, X. Liu, Z.-F. Li, P.-Y. Li, Y. Ma, C. Liu, P.-J. Liang, X. Li, Y.-X. Xiao, J. Hu, C.-F. Li, and G.-C. Guo, *Nature Communications* **9**, 3407 (2018).
- [49] M. Shah and L. Fan, *Physical Review Applied* **15**, 034071 (2021).
- [50] J. M. Lukens and P. Lougovski, *Optica* **4**, 8 (2017).
- [51] N. Maring, D. Lago-Rivera, A. Lenhard, G. Heinze, and H. de Riedmatten, *Optica* **5**, 507 (2018).
- [52] S. Zhou and L. Jiang, *Phys. Rev. A* **99**, 013808 (2019).
- [53] M. Tsang, *Phys. Rev. A* **99**, 012305 (2019).
- [54] J. Řeháček, Z. Hradil, D. Koutný, J. Grover, A. Krzic, and L. L. Sánchez-Soto, *Phys. Rev. A* **98**, 012103 (2018).
- [55] A. A. Pushkina, G. Maltese, J. I. Costa-Filho, P. Patel, and A. I. Lvovsky, Super-resolution linear optical imaging in the far field (2021), [arXiv:2105.01743](https://arxiv.org/abs/2105.01743).
- [56] M. Lipka, M. Parniak, and W. Wasilewski, *Applied Physics B* **123**, 238 (2017).
- [57] L. Neuhaus, R. Metzдорff, S. Chua, T. Jacqmin, T. Briant, A. Heidmann, P. Cohadon, and S. Deléglise, in *2017 Conference on Lasers and Electro-Optics Europe European Quantum Electronics Conference (CLEO/Europe-EQEC)* (2017).
- [58] L. Heller, P. Farrera, G. Heinze, and H. de Riedmatten, *Phys. Rev. Lett.* **124**, 210504 (2020).
- [59] X.-J. Wang, S.-J. Yang, P.-F. Sun, B. Jing, J. Li, M.-T. Zhou, X.-H. Bao, and J.-W. Pan, *Phys. Rev. Lett.* **126**, 090501 (2021).
- [60] Y. Jiang, Y. Mei, Y. Zou, Y. Zuo, and S. Du, *Review of Scientific Instruments* **90**, 013105 (2019).